J. Fluid Mech. (2007), *vol.* 574, *pp.* 59–84.
doi:10.1017/S0022112006004034 Printed in the United Kingdom

Direct numerical simulation of round turbulent jets in crossflow

SUMAN MUPPIDI AND KRISHNAN MAHESH

Aerospace Engineering and Mechanics Department, University of Minnesota,
Minneapolis, MN 55455, USA

(Received 28 March 2006 and in revised form 29 August 2006)

Direct numerical simulation is used to study a round turbulent jet in a laminar crossflow. The ratio of bulk jet velocity to free-stream crossflow velocity is 5.7 and the Reynolds number based on the bulk jet velocity and the jet exit diameter is 5000. The mean velocity and turbulent intensities from the simulations are compared to data from the experiments by Su & Mungal (2004) and good agreement is observed. Additional quantities, not available from experiments, are presented. Turbulent kinetic energy budgets are computed for this flow. Examination of the budgets shows that the near field is far from a state of turbulent equilibrium – especially along the jet edges. Also – in the near field – peak kinetic energy production is observed close to the leading edge, while peak dissipation is observed toward the trailing edge of the jet. The results are used to comment upon the difficulty involved in predicting this flow using RANS computations. There exist regions in this flow where the pressure transport term, neglected by some models and poorly modelled by others, is significant. And past the jet exit, the flow is not close to established canonical flows on which most models appear to be based.

1. Introduction

A jet in crossflow is defined as the flow field where a jet of fluid enters and interacts with a crossflowing fluid. Important examples of jets in crossflow are fuel injectors, smokestacks, film cooling on turbine blades and dilution holes in gas turbine combustors. Margason (1993) provides a comprehensive review of past work on this problem. The emphasis has been on the study of the velocity and vorticity fields (Kamotani & Greber 1972; Fearn & Weston 1974; Andreopoulos & Rodi 1984; Fric & Roshko 1994; Krothapalli; Lourenco & Buchlin 1990; Kelso & Smits 1995), the study of the scalar mixing (Smith & Mungal 1998; Su & Mungal 2004) and attempts at modelling the flow field and jet trajectory (Broadwell & Breidenthal 1984; Karagozian 1986; Hasselbrink & Mungal 2001; Muppidi & Mahesh 2005).

Some of the recent work on jets in crossflow involves numerical simulations. Calculations based on the Reynolds-averaged equations appear not to adequately predict the turbulent statistics (e.g Chochua *et al.* 2000). Two-equation models have also been shown to under-predict the lateral jet width, and over-predict the jet's penetration into the crossflow (Acharya, Tyagi & Hoda 2001). In comparison, large eddy simulations (LES) have provided better agreement with experimental data. Yuan and coworkers (Yuan & Street 1998; Yuan, Street & Ferziger 1999) performed LES of a round jet in crossflow under comparable conditions to experiments by Sherif & Pletcher (1989) and compared statistics of mean velocity, turbulent intensities

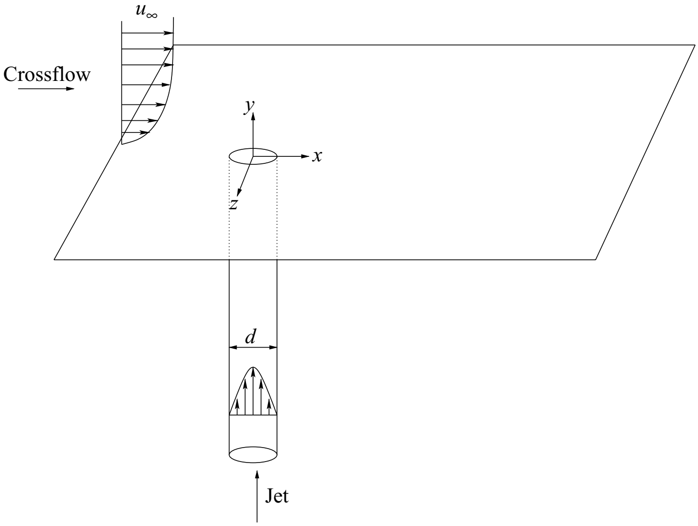

FIGURE 1. Schematic of the problem.

and passive scalar concentration. The LES was shown to reproduce the large-scale coherent structures observed experimentally, and their results were used to suggest that the upright vortices seen in the wake of the jet are related to the horseshoe vortices upstream of the jet. Mechanisms for jet bending and entrainment were also examined. Schluter & Schonfeld (2000) compared the results of their LES with experimental velocity profiles of Andreopoulos & Rodi (1984) and scalar fields of Smith & Mungal (1998), and obtained reasonable agreement.

The objective of this paper is to perform an experimentally validated DNS of a round turbulent jet in crossflow, to use the simulation to present statistics of quantities not available from the experiment, to examine the relevant time scales in this flow, and to discuss why typical RANS computations do not predict this flow field adequately. This paper is organized as follows. Section 2 describes the problem and the relevant parameters. Section 3 provides the details of the simulations. A few details of the flow field are presented in § 4.1. A comparison with the experimental data of Su & Mungal (2004) is presented in § 4.2 and the velocity field is discussed in § 4.3. Turbulent kinetic energy budgets for this flow are presented in § 5. The paper ends with a short summary in § 6.

2. Problem

Figure 1 shows a schematic of the problem, where a jet issues perpendicularly from a round pipe (of diameter d) into the crossflow. The crossflow is in the x-direction and the jet is in the y-direction. The origin is located at the centre of the jet exit as shown. Here u_∞ is the crossflow free stream velocity. The velocity ratio is defined as $r = \overline{u}_j/u_\infty$, where $\overline{u}_j$ is the mean jet velocity obtained by averaging u_j over the pipe cross-section.

Simulations are performed at the same conditions as the experiments by Su & Mungal (2004). The velocity ratio (r) is 5.7 and the Reynolds number of the flow, based on the bulk jet velocity and the jet–exit diameter, is 5000. In the experiment, the jet exits out of a round pipe (approximately 70 diameters long) into the crossflow. In the absence of any crossflow, fully developed pipe flow conditions are expected at the jet exit (Su & Mungal, § 2). The experiment considered two cases : one where the jet exit was flush with the wall and another where the pipe protruded into the crossflow. The present simulations are confined to the case of the jet exit flush with the wall, as shown in figure 1. The crossflow is laminar and the 80 % boundary layer thickness is $\delta_{80\%} = 1.32\,d$ at the location of the centre of the jet exit, and in the absence of the jet.

3. Simulation details

3.1. *Algorithm*

The numerical scheme solves the incompressible Navier–Stokes equations,

$$\frac{\partial u_i}{\partial t} + \frac{\partial u_i u_j}{\partial x_j} = -\frac{\partial p}{\partial x_i} + \nu \frac{\partial^2 u_i}{\partial x_j x_j}, \quad \frac{\partial u_i}{\partial x_i} = 0, \tag{3.1}$$

on unstructured grids, where u_i, p and ν denote the velocities, pressure and kinematic viscosity respectively. The density of the fluid is constant and is absorbed into the pressure. The numerical scheme is described by Mahesh, Constantinescu & Moin (2004) in detail. The scheme is a predictor–corrector formulation which is robust at high Reynolds numbers without numerical dissipation. The Cartesian velocities and the pressure are stored at the centroids of the control volumes and the face normal velocities are stored independently at the centroids of the faces. The predicted velocities at the control volume centroids are obtained using the viscous and the non-linear terms of (3.1) and are used to predict the face normal velocities on the faces. The predicted face normal velocity is projected so that continuity is discretely satisfied. The resulting Poisson equation for pressure is solved iteratively using a multigrid approach. The Crank–Nicolson scheme is used to advance implicitly in time. The algorithm has been validated for a variety of problems (see Mahesh *et al.* 2004) over a range of Reynolds numbers.

3.2. *Computational domain and boundary conditions*

The computational domain extends $36d \times 64d \times 64d$ in the axial, wall-normal and spanwise directions (x, y and z) respectively. Preliminary computations were performed to establish that a domain of this size does not constrain the jet, and that the flow does not feel the effects of confinement by the boundary. A pipe of length $2d$ is included in the computational domain in order to allow the fully developed turbulent pipe flow field (at the inlet) to adjust to the interaction between the jet and the crossflow. The crossflow inflow plane is located $4d$ upstream of the jet exit.

The crossflow is modelled as a laminar flow past a flat plate. In the absence of the jet, the crossflow has a boundary layer thickness of $\delta_{80\%} = 1.32d$ at the centre of the jet exit. At the crossflow inflow plane, the velocity field is specified as the solution to the Blasius boundary layer equation (Schlichting 1968). The inflow boundary layer thickness is specified such that the boundary layer grows to the required thickness at the jet exit in the absence of the jet. The boundary condition is validated by performing a simulation of only the crossflow, on a domain without the pipe. The mesh used for this validation study was considerably coarser (edge lengths 5–10 times in the streamwise and spanwise directions) than that used in the turbulent simulation. Figure 2(*a*) shows the results of this validation. Streamwise velocity u at all the control volumes of the domain is plotted against the similarity variable η (where $\eta = y\sqrt{u_\infty/\nu x}$). The symbols show the results from the simulation, and are compared to the analytical Blasius solution (shown as a solid line). Note that good agreement is obtained.

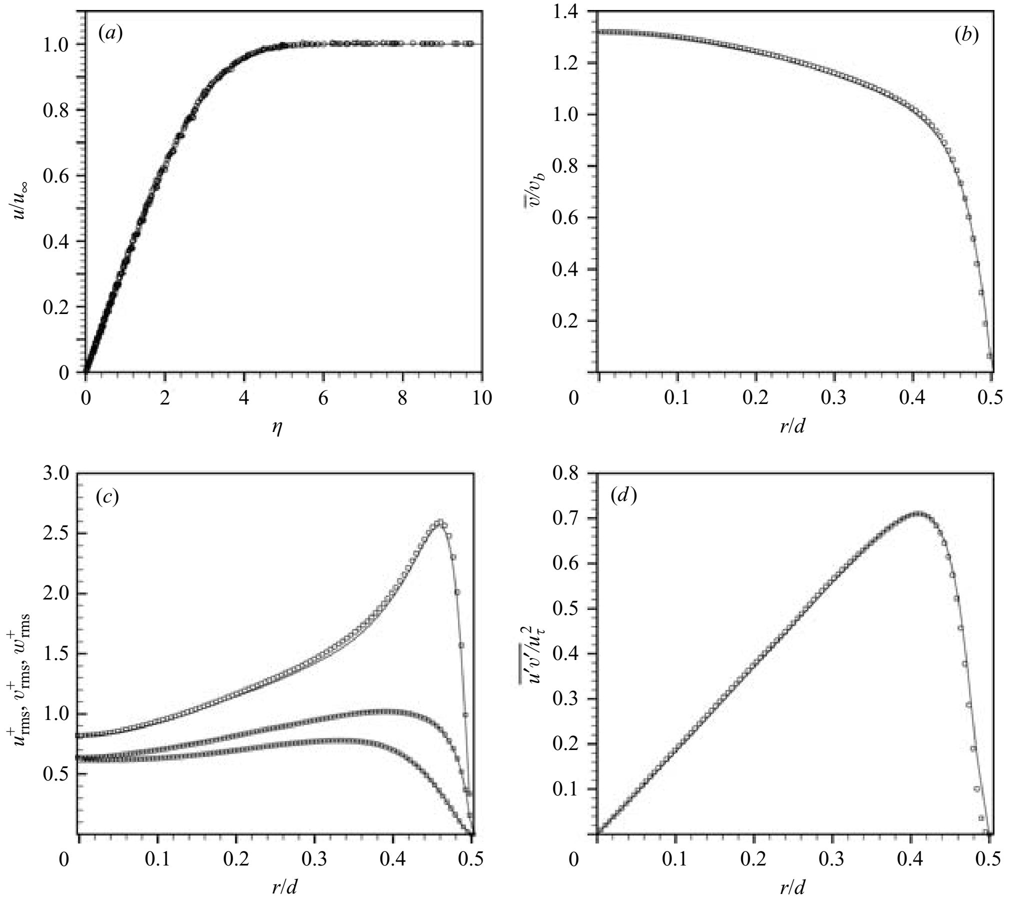

FIGURE 2. (*a*) Validation of the crossflow. Comparison with analytical Blasius solution. ○, simulations; ——, Analytical solution. (*b*), (*c*), (*d*) Validation of the turbulent pipe flow. Comparison to data from Eggels *et al.* (1994). ——, simulation; □, Eggels *et al.*

The jet in the experiment is turbulent and fully developed by the time the fluid exits the jet exit. A separate computation is therefore performed to simulate fully developed turbulent flow in a pipe. The Reynolds number (based on the pipe diameter and the mean axial velocity) is 5000. The computational mesh contained $256 \times 96 \times 128$ points in the axial, radial and the azimuthal directions respectively. In wall units, the grid spacing is $\Delta x^+ = 6.762$, $\Delta r^+ = 1.802$, and in the azimuthal direction, the minimum and maximum spacings are $\Delta\theta^+ = 0.0042$ and 8.447 respectively. Figures 2(*b*), 2(*c*) and 2(*d*) compare the radial profiles of velocity and turbulent intensities to the results of Eggels *et al.* (1994). Mean axial velocity $\overline{v}$ is normalized with the bulk velocity v_b (figure 2*b*), and the r.m.s. velocities and Reynolds shear stress (figures 2(*c*) and 2(*d*)) are normalized with the friction velocity ($u_\tau = \sqrt{\tau_{wall}/\rho}$, where τ_{wall} is the wall shear stress). The profiles shown in solid lines are from the present simulation and the symbols denote the results of Eggels *et al.* (1994). Note that good agreement is obtained.

Once the pipe flow simulation becomes statistically stationary, the instantaneous velocity field at a cross-sectional plane is stored over a length of time (over, approximately, 200 d/u_∞ units). The stored velocity field is interpolated onto the inflow plane of the jet in the turbulent jet simulation. On the exit plane ($x/d = 32$), a zero-gradient boundary condition is used for the velocities. On the spanwise boundaries ($z/d = \pm 32$), the velocity field corresponding to the laminar crossflow is specified. Free-stream velocity boundary conditions are specified on the top boundary ($y/d = 64$).

3.3. *Computational mesh*

The computational mesh is unstructured and consists of approximately 11 million hexahedral elements. The smallest elements are found at the walls of the pipe and the crossflow. The largest elements are found away from the jet exit and the wall. The mesh is constructed as follows. The inflow plane for the pipe ($y/d = -2$) is first meshed; 128 elements are used in the azimuthal direction and 72 elements in the radial direction (up to a depth of about $0.4d$ inwards from the wall). This part of the face mesh is structured. The rest of the plane is meshed using unstructured elements of size (edge length) $0.005d$. This face mesh is now swept in the y-direction up until the jet–exit ($y/d = 0$) with an edge length (Δy) of $0.02d$. Note that the mesh in this part of the domain is based on the mesh used to simulate the turbulent pipe flow specified at the inlet.

The wall of the crossflow is then meshed. The size of the mesh elements in the region around the jet exit is allowed to grow (with 128 azimuthal elements) linearly outward at a ratio of 1.05. This is done until the elements grow to an edge length of $0.1d$. The region of interest, roughly spanning $5d$ either side of the symmetry plane and up to $20d$ downstream of the jet exit, is meshed using unstructured elements of size 0.1–$0.15d$. The rest of the plane is then meshed with elements that are allowed to be large away from the region of interest. Mesh elements of around $1.0d$ are found at distances about $24d$ away from the symmetry plane and around $24d$ downstream of the jet exit. The mesh size variation is not allowed to be unreasonably high anywhere in or near the region of interest. The mesh on the plane $y/d = 0$ is now swept in the y-direction. A boundary layer at the crossflow wall allows fine elements near the wall ($\Delta y = 0.01d$) and the mesh size increases linearly away from it at a rate of 1.05 till the mesh size is $0.1d$. Δy is kept constant until a height of $y/d = 24$. Past this plane (note that jet exits the domain before crossing this plane), Δy is allowed to grow linearly at a rate of 1.1.

The computational domain, mesh and the boundary conditions were chosen after a series of simulations. For example, simulations were performed on domain sizes of $36d \times 32d \times 12d$ and $36d \times 64d \times 12d$ before the present simulation where the domain is $36d \times 64d \times 64d$. The computational mesh used in the preliminary simulations initially contained 2.4 million elements, which was refined to 6 million, 8 million, and finally the present mesh which contains about 11 million elements. Preliminary simulations of a laminar jet in crossflow were performed on a domain that included a $10d$ length of pipe. An examination of the velocity profile in the pipe showed that at $r = 5.7$, a pipe of length $2d$ is sufficient to let the jet evolve naturally before exiting into the crossflow.

4. Flow field

The simulation is performed at a time step of 0.0025 non-dimensional time units (d/u_∞). The computation is begun with a 'no-flow' initial condition. The solution is allowed to evolve until about 80 time units, by which time the transients exit the computational domain. Statistics, presented in this paper, are then computed over

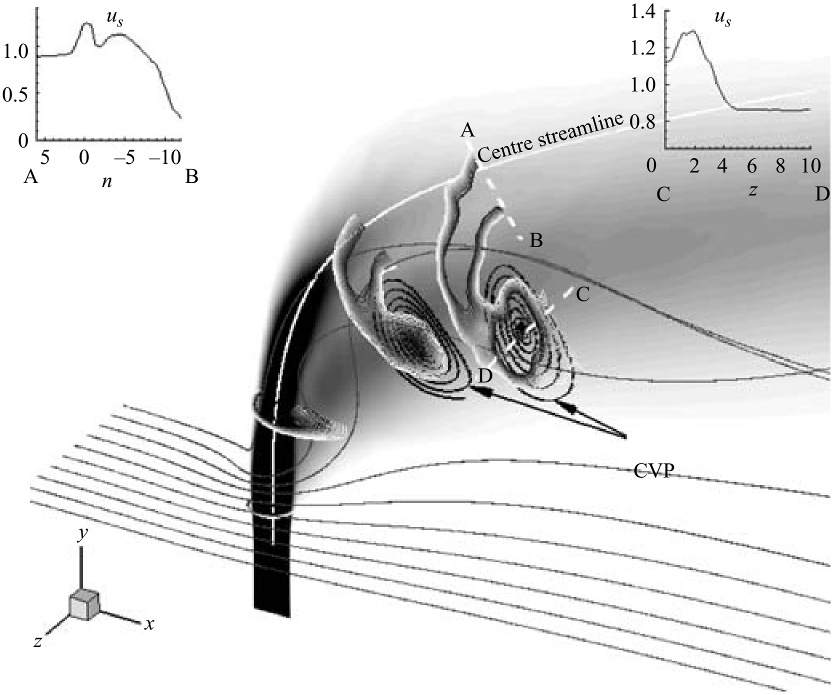

FIGURE 3. Isometric view of the flow field. Contours of velocity $\langle v \rangle$ on the symmetry plane indicate the extent of the jet. Centre streamline is shown in white. Jet cross-section, at $s = d$, $4d$, $10d$ and $15d$, is shown using contours of $\langle u_s \rangle$. Streamlines at these locations indicate the stages of CVP formation. Streamlines originating in the crossflow fluid show entrainment of the crossflow fluid by the jet.

another 120 time units. Statistical convergence is ensured by comparing the statistics computed using increasing number of samples (and hence increasing flow time over which statistics are computed). The profiles presented are computed over 120 units of time, and using 12 thousand samples.

4.1. *Evolution of the jet*

As a jet issues into the crossflow, it deflects in the direction of the crossflow. Additionally, a pair of counter-rotating vortices is generated. The counter-rotating vortex pair (CVP) has been considered to be a dominant feature of this flow and has been observed to persist far downstream (Keffer & Baines 1963; Pratte & Baines 1967; Kelso, Lim & Perry 1996). It is convenient to study the evolution of the jet in a coordinate system that is aligned with the jet. At any point along the jet trajectory (defined by the centre streamline), a new coordinate system s–n is obtained by rotating the x–y axes about the z-axis by an angle θ. On the s–n plane, s is the coordinate along the jet centreline, and n is the coordinate normal to the centreline. The z-coordinate is the same in both the coordinate systems. By a simple coordinate transformation, the velocity field can be expressed in terms of u_s, u_n and w, along the s-, n- and z-axes respectively.

Figure 3 presents an isometric view of the flow field. Time-averaged contours of velocity v on the symmetry plane give an indication of the extent of the jet. The centre streamline, shown in white, passes through the centre of the jet exit. Note that the jet is wider toward the leeward side than toward the windward side of the centre streamline. This disparity has been noted by Su & Mungal (2004, figure 8). Figure 4 shows three-dimensional streamlines that originate in the pipe, indicating the motion of the jet fluid. The centre streamline (shown as a thick line) originates at the centre of the jet exit. All the other streamlines originate along the edge of the jet (near the walls of the pipe). The trajectories of streamlines that do not originate on the symmetry plane are shallower than the trajectory of the centre streamline. This results in the jet being wider on the leeward side of the centre streamline. Also note that the crossflow fluid has a higher momentum at the upstream side of the jet (negative x side of the jet centreline) as compared to the downstream side of the jet. This difference in momentum could also aid in accentuating the asymmetry in the jet width. This feature is also observed instantaneously.

At distances of $s = d$, $4d$, $10d$ and $15d$, the jet cross-section is presented (in figure 3) using contours of time-averaged trajectory-parallel velocity $\langle u_s \rangle$. With increasing s, an increase in size of the jet cross-section is observed, along with a change in shape. Close to the jet exit, the jet cross-section is circular, and fluid with the highest velocity is seen towards the centre. The trailing edge flattens as the jet cross-section deforms to a kidney shape. Away from the jet exit, the high velocity contours are seen toward the edges of the jet, while the fluid towards the centre appears to have a relatively lower velocity. At these cross-sections, streamlines show the stages of formation of the CVP. At $s = d$, streamlines show a small region of vorticity toward the trailing edge of the jet. Moving farther, the CVP increases in size. At $s = 15d$, figure 3 shows profiles of $\langle u_s \rangle$ along the n-axis (A–B) and along the z-axis (C–D). Note that the centre of the CVP corresponds to peak $\langle u_s \rangle$ along C–D. Along the line A–B (from the windward side of the jet toward the centre and beyond), $\langle u_s \rangle$ begins to increase near the jet edge, reaches a peak near the jet centre, decreases, and exhibits a second peak below the jet centreline.

The centre of the CVP (where the vorticity is maximum) lies below (positive x, negative y side) the centre streamline, as observed in figure 3. This supports the observation (Fearn & Weston 1974) that a jet trajectory based on the centre streamline penetrates deeper into the crossflow than a trajectory based on vorticity. Owing to the CVP and to lower fluid velocities near the centre of the jet cross-section, it may be expected that the scalar gets 'trapped' in this region of low velocity, and that more of the fluid containing the scalar would be present below the centre streamline than above. As a consequence, a trajectory based on the scalar concentration would penetrate less into the crossflow than a trajectory based on the centre streamline, as observed by Kamotani & Greber (1972), Yuan & Street (1998) and Su & Mungal (2004). As s increases, so does the displacement between the centre streamline and the CVP, suggesting that the difference between trajectories increases along the length of the jet. Figure 3 also shows a few representative streamlines. These originate from the crossflow inflow plane, and describe the motion of the crossflow fluid. Crossflow fluid travels around the jet, and some of it is entrained by the jet on the downstream side. These streamlines hint that the jet entrains more crossflow fluid on the downstream side than on the upstream side. Finally, the fact that the streamlines do not just follow the centre streamline, that they exhibit a significant curvature (figures 3 and 4), indicates the effect of the CVP and the strength of its vorticity.

4.2. *Comparison with experiments*

Su & Mungal (2004) provide detailed experimental profiles of velocity and turbulent intensities at a few horizontal stations, as a function of the non-dimensionalized

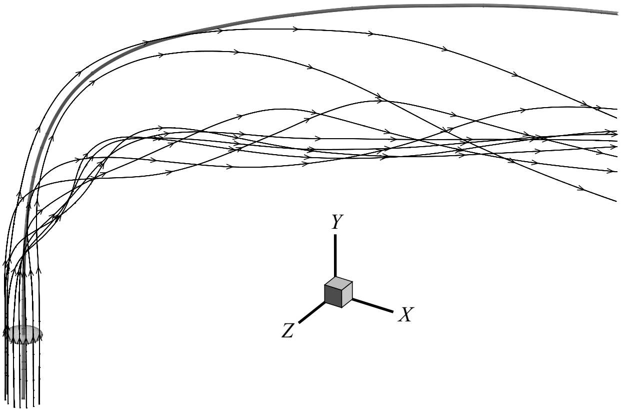

FIGURE 4. Three-dimensional streamlines originating inside the pipe.

streamwise distance (x/rd), along with the mean jet trajectory. This subsection compares results from the simulation to that of the experiment.

Su and Mungal report that the bulk jet velocity ($\overline{u_j}$) in their experiment is 16.9 m s^{-1} and that the free-stream crossflow velocity (u_∞) is 2.95 m s^{-1}, which gives a velocity ratio ($r = \overline{u_j}/u_\infty$) of 5.7. The velocity ratio in the simulation is also 5.7. The Reynolds number based on the bulk jet velocity and the jet exit diameter is 5000, and matches that in the experiment. Note that the simulation assumes both the jet fluid and the crossflow fluid to have the same density. However, in the experiment, the jet fluid (nitrogen) is seeded with acetone vapour which gives the jet fluid a 10 % higher density ($\rho_j/\rho_\infty = 1.1$, Su & Mungal 2004). If the velocity ratio (r_{eff}) were to be defined based on the momentum

$$r_{eff}^2 = \frac{\rho_j \overline{u_j}^2}{\rho_\infty {u_\infty}^2} = \frac{\rho_j}{\rho_\infty} r^2, \tag{4.1}$$

the flow parameters described in Su & Mungal (2004) yield a $r_{eff} = 6.008$. It has been previously noted (Muppidi & Mahesh 2005) that the flow field of a jet in crossflow is very sensitive to the jet inflow at the jet exit. As a jet of fluid with a density 10% higher than that of the crossflow exits the jet exit, it has a momentum that is 10% higher than a jet with the same fluid density as that of the crossflow. This higher momentum could lead to higher peak velocities ($\overline{v}$), sharper intensity gradients and a trajectory that penetrates deeper into the crossflow.

Figure 5(*a*) compares the experimentally observed jet trajectory to the trajectory extracted from the simulation. The axes are normalized by r. Note that the jet in the experiment penetrates deeper into the crossflow. It should be mentioned here that the jet trajectory from the experiment is extracted using the local scalar maxima, and the trajectory from the present computation is defined based on the streamline passing through the jet exit on the symmetry plane. It has been shown (Su & Mungal 2004, figure 19) that the trajectory based on the centre streamline penetrates deeper into the crossflow than the trajectory based on the local scalar maxima. Figure 5(*a*) shows, however, that owing to the difference in the densities, the trajectory based on the centre streamline is lower than the scalar maxima trajectory from the experiment.

A reasonable approach to compare the experimental and computed results is to use r_{eff} to scale the results instead of r. Such a scaling would account for the density ratio of the jet and the crossflow fluids. Jet trajectories scaled using r_{eff} are shown in figure 5(*b*); $r_{eff} = 5.7$ for the simulation and $r_{eff} = 6.008$ for the experiment, a difference

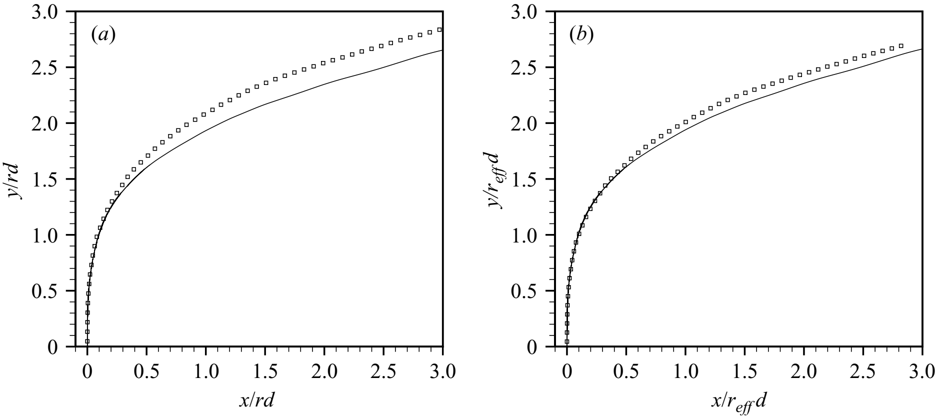

FIGURE 5. Comparison of jet trajectory from the simulation (———) with that from the experiment (□); (*a*) scaled using r, and (*b*) scaled using r_{eff}.

of approximately 5%. It is observed that rescaling the trajectories brings them closer to each other. At a location $15d$ downstream of the jet exit, the difference between the trajectories scaled with rd is about 6.5 % while scaling the trajectories using $r_{eff}d$ reduces the difference to 2.8%.

Figure 6 compares profiles of $\overline{v}$ and $\overline{v'v'}$ between the simulation and the experiment, while profiles of $\overline{u'u'}$ and $\overline{u'v'}$ are compared in figure 7. The solid lines in these plots are results from the present simulation while the symbols are results from the experiment. In order to account for the difference in jet fluid density, the velocity and turbulent intensities are scaled using r_{eff}.

Close to the jet exit, the jet shows characteristics similar to that of turbulent flow in a pipe. Both $\overline{v}$ and $\overline{v'v'}$ appear to be symmetric about $x=0$. One difference from a turbulent pipe flow profile is a small negative velocity $\overline{v}$ upstream of the jet (peak negative velocity is observed at $x\sim -0.1rd$). The crossflow fluid sees the jet as an obstacle, resulting in a high-pressure region upstream of the jet (profiles of pressure are shown in figure 11*c*). This pressure gradient forces crossflow fluid towards the jet exit (the crossflow fluid even enters the pipe at sufficiently small velocity ratios), giving rise to the negative $\overline{v}$ as observed. Similar behaviour is observed when the jet is laminar (Muppidi & Mahesh 2005). Moving away from the jet exit, the profiles lose the symmetry. At the farthest station ($y/rd=1.0$), the observed profile for $\overline{v}$ appears to be composed of two distinct jets, one with a higher velocity (centred at $x=0.1rd$) followed by another with a lower velocity (centred at $x=0.38rd$). Section 4.1 mentioned the jet fluid on the sides of the jet that is deposited on the symmetry plane downstream of the jet. This jet fluid possesses a vertical velocity and results in a ‘two-jet’ profile as observed.

In comparison to $\overline{v}$ and $\overline{v'v'}$, the streamwise velocity at the leading and the trailing edges of the jet is different, and hence the profile of $\overline{u'u'}$ is not symmetric even at the $0.1rd$, the station closest to the jet exit. Moving away from the jet exit, the turbulent intensity profiles $\overline{u'u'}$ and $\overline{v'v'}$ show a single peak. As the jet begins to bend in the direction of the crossflow, moving away from the wall, the peak velocity and intensities are observed downstream of the jet exit. It must be mentioned here that the symmetry (about $x=0$) seen in the profiles of $\overline{v}$ and $\overline{v'v'}$ (at $0.1rd$) might not always be observed, particularly at lower r. It is known that at lower velocity ratios, the pressure gradient imposed on the jet by the crossflow might succeed in

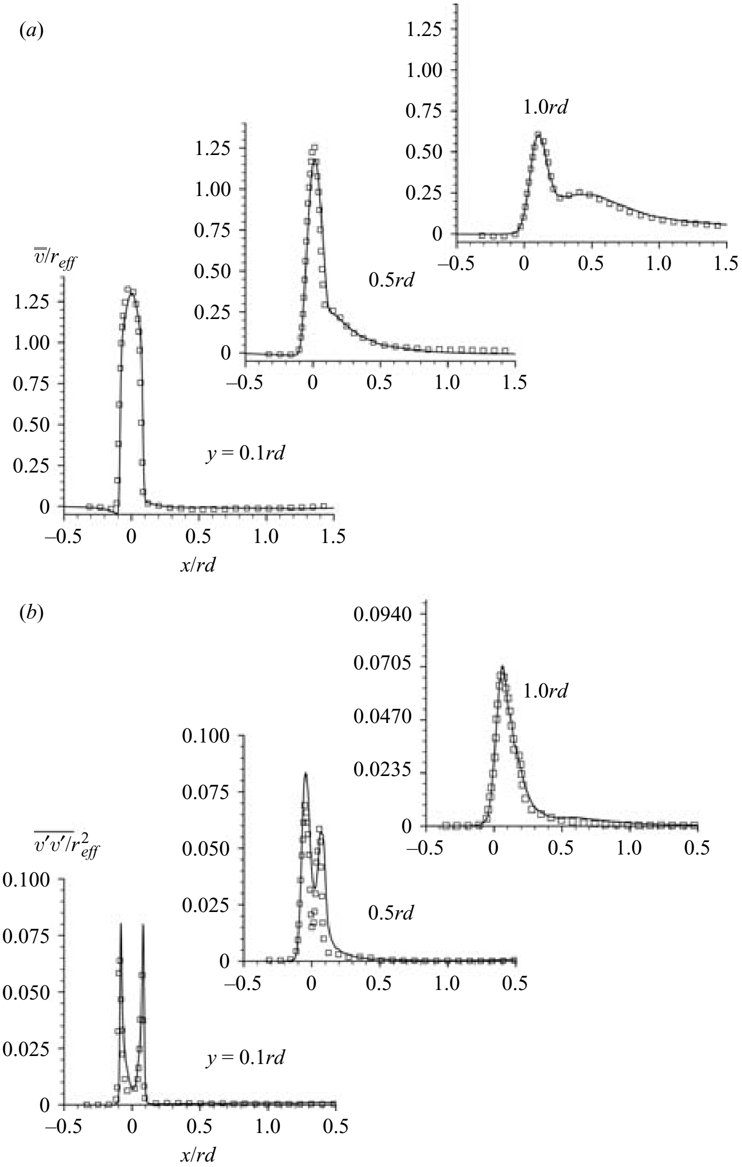

FIGURE 6. Comparison of mean vertical velocity ($\overline{v}$) and turbulent intensity ($\overline{v'v'}$) profiles with the experimental results. ———, simulation; □, experiment. Profiles belong to the symmetry plane, and at stations $y = 0.1rd$, $0.5rd$ and $1.0rd$.

forcing crossflow fluid into the pipe. Consequently, at lower velocity ratios (Muppidi & Mahesh 2005; the velocity ratio was 1.52), $\overline{v}$ is not symmetric at the jet exit. It must be expected that at such a r, even the turbulent intensity $\overline{v'v'}$ would not be symmetric. However, it appears from figure 6 that at this velocity ratio of 5.7, and at $y/rd = 0.1$, the profiles of $\overline{v}$ and $\overline{v'v'}$ are fairly symmetric.

Figure 7(*b*) shows a comparison of $\overline{u'v'}$. At the first two stations, a very good agreement is observed, while the profiles at the farthest station show a difference. While the location of the peaks appear to coincide, magnitude of peak $\overline{u'v'}$ from the experiment is higher than that from the simulation.

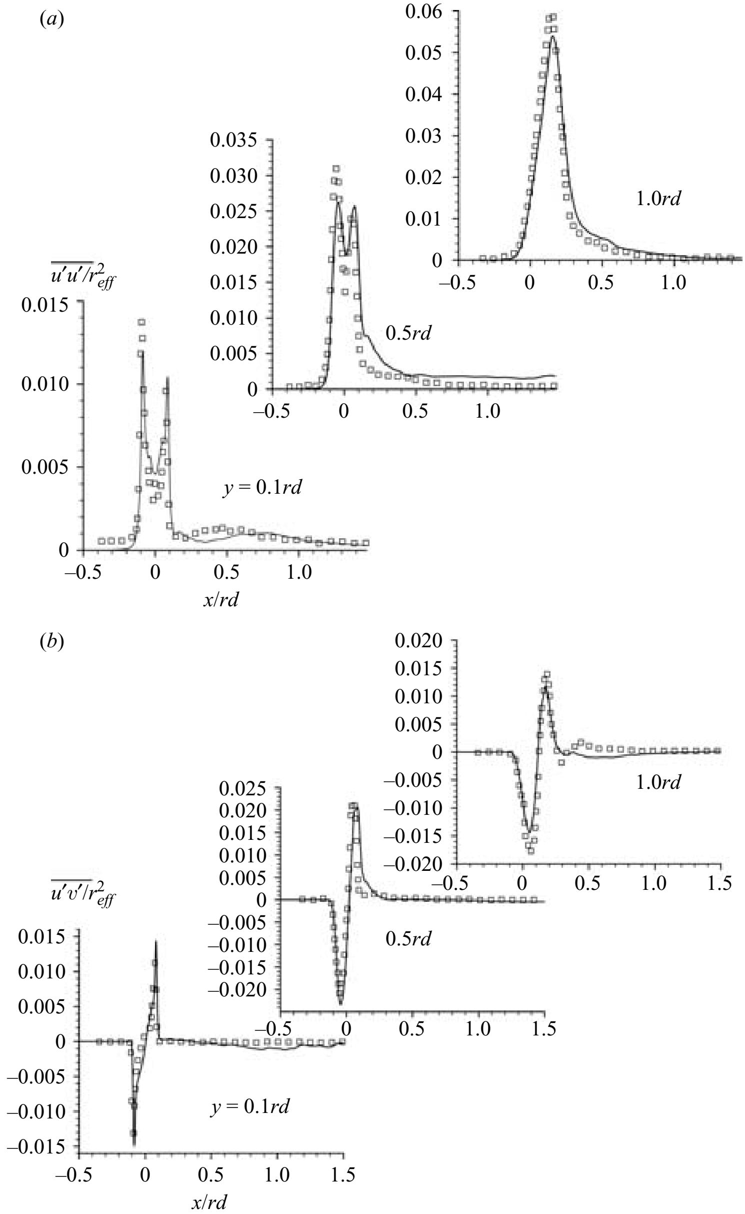

FIGURE 7. Comparison of mean turbulent intensity ($\overline{u'u'}$ and $\overline{u'v'}$) profiles with the experimental results. ———, simulation; □, experiment. Profiles belong to the symmetry plane, and at stations $y = 0.1rd$, $0.5rd$ and $1.0rd$.

Overall, for all the quantities compared and at all the locations, the agreement presented is quite reasonable, particularly, when seen in the context of the sharp gradients that the profiles possess (e.g. $\overline{v'v'}$ and $\overline{u'v'}$ at $y/rd = 0.1$).

4.3. *Velocity field*

Figure 8(*a*) shows the instantaneous contours of the magnitude of vorticity $\sqrt{\omega_x^2 + \omega_y^2 + \omega_z^2}$, non-dimensionalized using u_∞ and d, on the symmetry plane. The

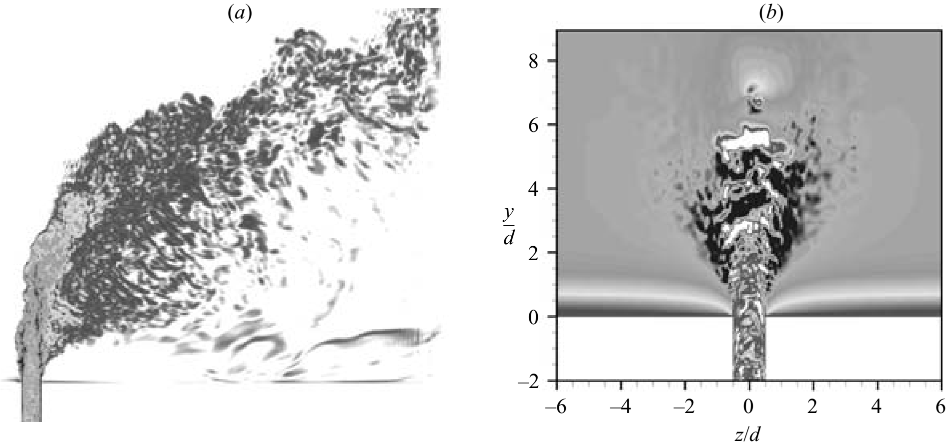

FIGURE 8. (*a*) Instantaneous contours of vorticity magnitude $\sqrt{\omega_x^2+\omega_y^2+\omega_z^2}$ on the symmetry plane. (*b*) Instantaneous contours of streamwise velocity u. End view at the jet exit($x/d=0$).

highest vorticity magnitude is observed near the walls of the pipe and along the jet. Note the small scales of motion inside the pipe and close to the jet exit. Small scale features are observed even away from the jet exit along the jet centreline, though the vorticity magnitude is lower. Upstream of the jet, the crossflow fluid shows a vorticity that is steady, smaller in magnitude, and characteristic of a laminar boundary layer. Downstream of the jet (and $x/d<6$), there appears to be a quiescent region with low vorticity (shown in white). Further downstream, the flow contains larger-scale features which move slowly in the direction of the crossflow. Instantaneous contours of the streamwise velocity (u) on the end-on plane ($x/d=0$) are shown in figure 8(*b*). The direction of the crossflow fluid, in this figure, is into the plane of the paper. Small-scale flow features are clearly seen inside the pipe and near the jet exit as the jet fluid exits into the crossflow. The three-dimensionality of the flow field is apparent. Outside this interaction region (past about 5 diameters away from the jet exit), the crossflow fluid appears relatively quiescent. The contours show that the crossflow boundary layer thickness decreases close to the jet exit. This is due to the acceleration of the crossflow fluid as it travels around the jet.

The inflow condition at the pipe entrance is a time-dependent velocity field from the computation of a fully developed turbulent flow in a pipe. A pipe of length $2d$ is included in the domain to allow the jet to develop naturally prior to exiting into the crossflow. Figure 9(*a*) shows mean velocity ($\overline{v}$) profiles on the symmetry plane across the pipe diameter at different stations parallel to the x-axis; $y/d=-2, -1, 0, 1, 2$, and 3. Note that the first three profiles shown ($y/d=-2, -1$ and 0) do not differ much from each other. This would suggest that the length of pipe used in the computations is sufficient to model the problem. The jet decelerates as it interacts with the crossflow, and the momentum of the crossflow forces the jet to move to the right. As a result, the profiles show that, moving away from the jet exit, the peak velocity decreases and the peak shifts to the right. Profiles of turbulent intensity ($\overline{v'v'}$) are presented in figure 9(*b*). Once the fluid exits the jet and interacts with the crossflow, there is a significant increase in the turbulent intensity as is clearly seen. As with profiles of $\overline{v}$, locations of peak $\overline{v'v'}$ shift in the direction of the crossflow. Along the length of the pipe ($y/d=-2, -1$ and 0), profile of $\overline{v'v'}$ shows a change more noticeable than

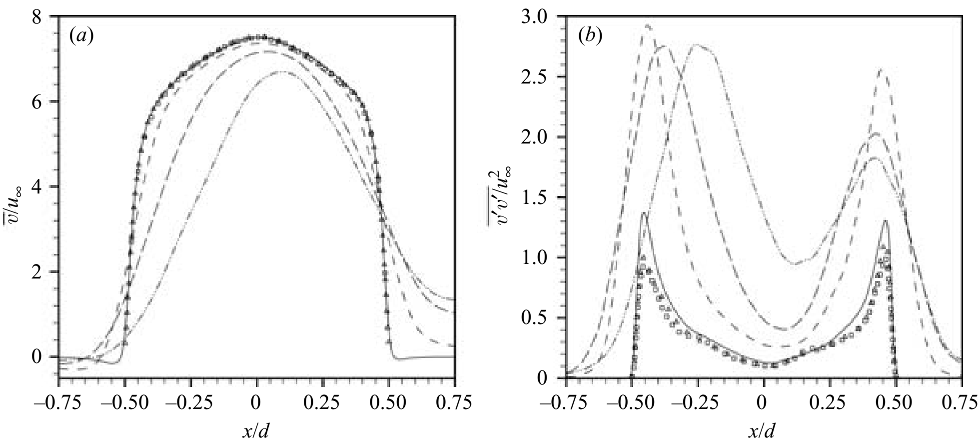

FIGURE 9. Profiles of velocity ($\overline{v}$) and turbulent intensity ($\overline{v'v'}$) across the jet diameter at different stations parallel to the wall : □ $y/d = -2$, △, -1; ——, 0; ----, 1; — — —, 2; —··—, 3.

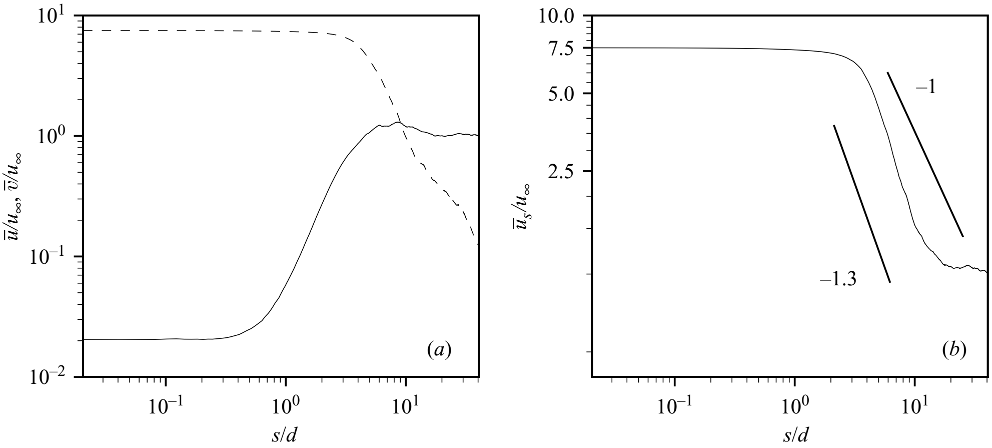

FIGURE 10. Variation of velocities along the centre streamline, plotted as a function of distance from the jet exit (a) ——, $\langle u \rangle$ and ----, $\langle v \rangle$, and (b) $\langle u_s \rangle$. The thick lines show slopes of -1 and -1.3.

that observed in the profile of $\overline{v}$. Such a change in $\overline{v'v'}$ shows that the fluid in the pipe is adjusting to the interaction past the jet exit. This behaviour makes the case for simulating the flow in the pipe upstream of the jet exit. This aspect has been previously mentioned in Yuan *et al.* (1999) and Muppidi & Mahesh (2005).

Figure 10(*a*) shows the variation of the horizontal and vertical components of mean velocity ($\langle u \rangle$, $\langle v \rangle$) along the centre streamline. The coordinate $s = 0$ corresponds to the jet exit. In the near field, the direction of the jet fluid is essentially vertical, and is reflected in the fact that $\langle v \rangle$ is greater than $\langle u \rangle$ by a couple of orders of magnitude at low s. As the jet evolves and bends, the jet fluid accelerates in the direction of the crossflow fluid, indicated by the increase in $\langle u \rangle$. In the far field, one would expect the jet fluid to travel in the direction of the crossflow, and hence the asymptotic values of the curves would be u_∞ for $\langle u \rangle$ and zero for $\langle v \rangle$.

Variation of the trajectory-parallel component of velocity $\langle u_s \rangle$, along the jet length, is plotted in figure 10(*b*). Note that by definition,

$$\langle u_s \rangle = \sqrt{\langle u \rangle^2 + \langle v \rangle^2}, \tag{4.2}$$

since the trajectory-normal component ($\langle u_n \rangle$) is zero. The velocity decay is plotted on a log–log graph along with slopes of −1 and −1.3. For a regular turbulent jet, the velocity decay occurs at a rate of −1, i.e. $u_s \propto 1/s$. From figure 10(*b*), it appears that the centreline velocity decays at a rate faster than $1/s$ and that the decay rate is closer to −1.3. This faster decay rate only confirms that a transverse jet mixes better/faster with the crossflow fluid than does a regular jet with the ambient fluid. Past about $10d$, the decay rate falls and it appears that u_s approaches u_∞. Smith & Mungal (1998) use a 'branch point' to differentiate between the near field and the far field. From the results of experiments at a range of r, the branch point is posited to be at $s = 0.3r^2d$ ($s = 9.75d$, for $r = 5.7$). Their results of scalar concentration decay show a −1.3 decay in the near field and a −2/3 decay rate in the far field. In contrast to Smith & Mungal's results, Su & Mungal (2004) observe a scalar concentration decay rate of $1/s$ in the near field and higher decay rate past $s \sim 2.5rd$ ($s \sim 14.25d$; $s/r^2d \sim 0.44$). Su & Mungal also present the decay of magnitude of velocity with s. As mentioned earlier, along the jet centre streamline, this quantity is equal to u_s. Their results show a behaviour similar to the present results: the decay rate is visibly faster than $1/s$ in the near field and the velocity asymptotically approaches the free-stream crossflow velocity in the far field.

Figure 11 contains horizontal profiles of a few other quantities on the symmetry plane. Mean vorticity $\langle \omega_z \rangle$ and spanwise velocity variance $\langle w'w' \rangle$ are plotted, along with mean pressure $\langle p \rangle$ and $\langle p'p' \rangle$. As earlier, the horizontal profiles correspond to vertical locations $y/rd = 0.1, 0.5$ and 1.0. Profiles of mean vorticity show that both the peak magnitude and the steepness of the curves decrease from $y = 0.1rd$ to $0.5rd$ to $1.0rd$. Past the jet width (both upstream and downstream), the profiles indicate little vorticity. At the crossflow boundary, the pressure is the free-stream pressure. An increase in pressure is observed moving toward the jet and a peak $\overline{p}$ is seen just upstream of the jet exit. The crossflow exerts a favourable pressure gradient on the jet, as the profiles clearly show. This pressure gradient accelerates the jet fluid in the direction of the crossflow and suggests that the jet fluid can be considered as subject to an sudden acceleration (in the x-direction) once past the jet exit. The observed pressure gradient can be imagined to be a consequence of obstruction to the crossflow, and hence should scale with the crossflow velocity. Since the first of the profiles is within the crossflow boundary layer (where the crossflow velocity is lower than u_∞), it follows that the peak pressure observed at this station is lower than that observed further from the wall. The pressure minima correspond to the centre of the jet, downstream of which there is a region of pressure recovery.

Profiles of intensities of pressure and spanwise velocity, in figures 11(*b*) and 11(*d*) show steep gradients near the jet edges at the closest station. These profiles, along with the profiles of $\overline{u'u'}$, $\overline{v'v'}$ and $\overline{u'v'}$ shown earlier, indicate the high turbulent activity in the near field. Note that $\overline{p'p'}$ is asymmetric even at $y/rd = 0.1$, like $\overline{u'u'}$. At $y/rd = 0.5$, the difference in peak $\overline{p'p'}$ between the leading and trailing edges appears comparatively higher than that observed in $\overline{u'u'}$, $\overline{v'v'}$ or $\overline{w'w'}$. Also, $\overline{w'w'}$ shows a tertiary peak at $y/rd = 0.5$, corresponding to $x/rd \sim 0.23$. Recall, from §4.2 and figure 8 that jet fluid (from the sides of the jet) is deposited downstream of the jet

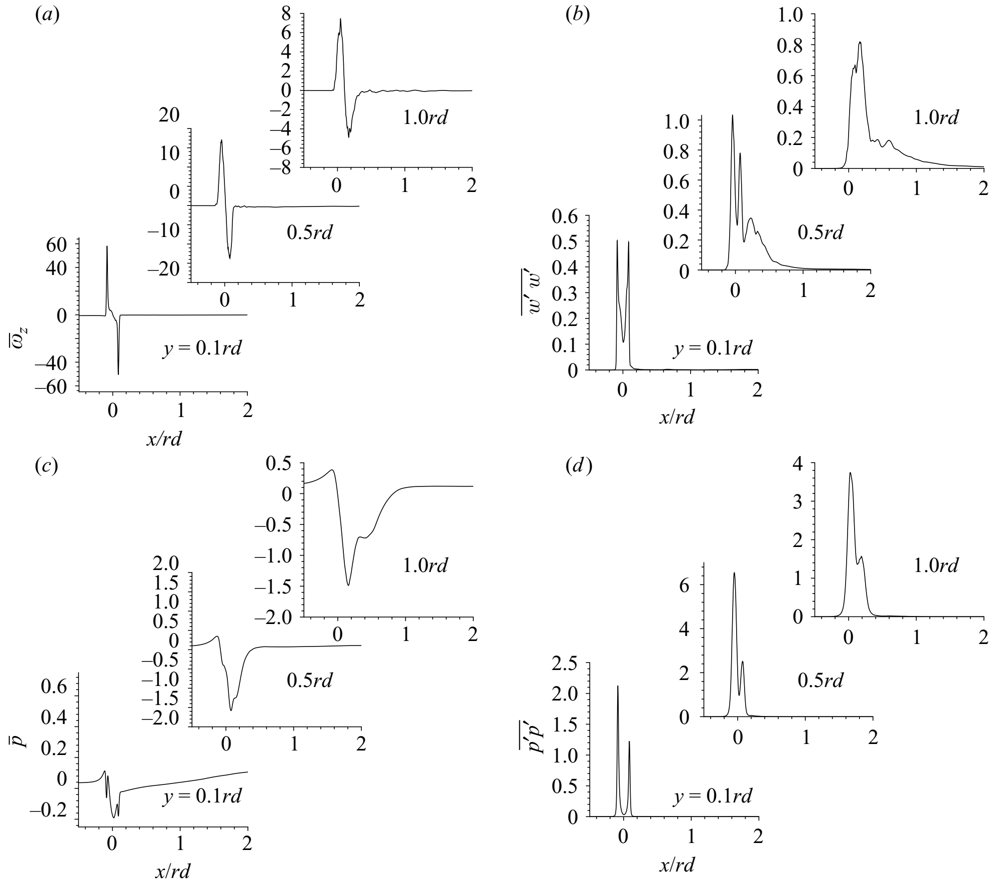

FIGURE 11. Horizontal profiles of (*a*) $\langle\omega_z\rangle$, (*b*) $\langle w'w'\rangle$, (*c*) $\langle p\rangle$ and (*d*) $\langle p'p'\rangle$ at locations $y/rd = 0.1, 0.5$ and 1.0.

by the crossflow fluid. Examination of $\overline{w'w'}$ contours on the symmetry plane indicates that the observed tertiary peak results from this feature of the flow.

5. Turbulent kinetic energy and budgets

Contours of the turbulent kinetic energy $k = \langle u_i u_i/2\rangle$ on the symmetry plane are shown in figure 12(*a*). Here, and in the rest of the paper, u_i indicates the fluctuating velocity, k is non-dimensionalized with the square of the velocity ratio i.e. $k/r^2u_\infty^2$. The mean jet trajectory is also shown. Yuan *et al.* (1999) present a similar plot from their simulation ($r = 3.3$, figure 23 in their paper) where the minimum and maximum values of $k/u_\infty^2 r^2$ are 0.01 and 0.1 respectively. The maximum $k/u_\infty^2 r^2$ inside the pipe is about 0.045, and is observed close to the wall. As the jet exits into the crossflow, the interaction between the jet and the crossflow fluids causes the turbulent kinetic energy to increase. Past the jet exit, the peak k is observed at the leading and trailing edges of the jet. Peak k at the leading edge is slightly higher than that at the trailing edge. Around $y/d \sim 2.5$, the shear layers corresponding to peak k on the leading and the trailing edges collapse. Downstream of this point, the jet exhibits a single peak, roughly along the mean jet trajectory.

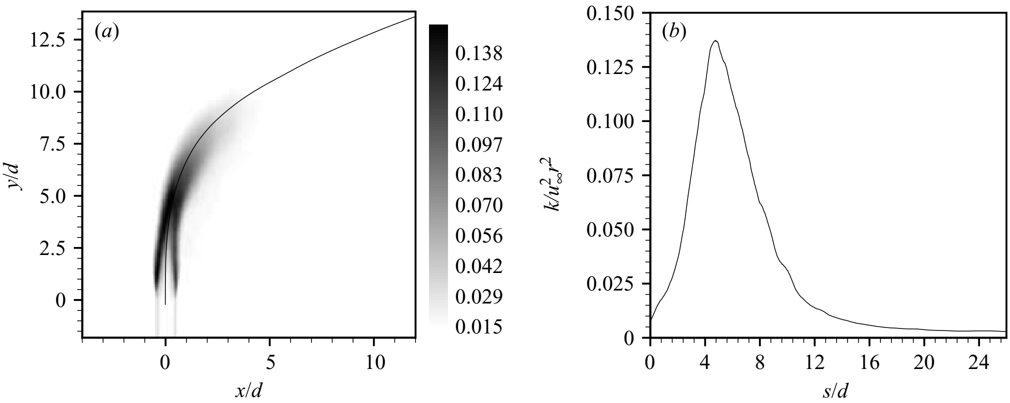

FIGURE 12. (*a*) Turbulent kinetic energy k/r^2 on the symmetry plane. Also shown is the centre streamline to indicate mean jet trajectory. (*b*) Variation of k along the centre streamline.

Figure 12(*b*) shows the variation of turbulent kinetic energy along the centre streamline. It is observed that, past the jet exit, the turbulent kinetic energy increases up to $s \sim 5d$ (where $k/u_\infty^2 r^2 \sim 0.135$) and begins to decrease thereafter. The variation of k with axial distance in a round turbulent jet shows a similar qualitative behaviour: k is highest near the edges of the jet, initially; along the axis, k increases with distance from the jet exit, peaks, and then decreases. At a Reynolds number of 2400, results from Babu & Mahesh (2004) show a peak k (non-dimensionalized with mean jet exit velocity) of around 0.038 at a distance of 7.5 diameters downstream of the jet exit.

The budget equation for the turbulence kinetic energy $k = \langle u_i u_i/2 \rangle$ may be written as

$$\underbrace{\frac{\partial}{\partial t}k + U_j \frac{\partial}{\partial x_j}k}_{\text{convection}} = \underbrace{-\langle u_i u_j \rangle \frac{\partial U_i}{\partial x_j}}_{\text{production}} \underbrace{-\nu \left\langle \frac{\partial u_i}{\partial x_j}\frac{\partial u_i}{\partial x_j} \right\rangle}_{\text{dissipation}} \underbrace{-\frac{1}{2}\frac{\partial}{\partial x_j}\langle u_i u_i u_j \rangle}_{\text{turbulent transport}} + \underbrace{\nu \frac{\partial^2}{\partial x_j \partial x_j}k}_{\text{viscous diffusion}} - \underbrace{\frac{1}{\rho}\frac{\partial}{\partial x_i}\langle u_i p \rangle}_{\text{pressure transport}} . \tag{5.1}$$

The budget terms have dimensions of velocity^2/time, and can be non-dimensionalized using d/u_∞^3. In the rest of the paper, P_{ii} denotes the non-dimensional production term, C_{ii} the non-dimensional convection and ϵ_{ii} denotes the non-dimensional dissipation. Non-dimensional pressure transport, turbulent transport and viscous diffusion are denoted by π_{ii}, T_{ii} and D_{ii} respectively. Figure 13 shows contours of P_{ii}, T_{ii}, π_{ii} and ϵ_{ii} on the symmetry plane. All the terms indicate little activity in the pipe (as compared to downstream of the jet exit) confined to a thin region near the pipe wall. The magnitude of all the terms, except D_{ii}, increase past the jet exit. As in figure 12 showing k, the peak budget terms appear to correspond to the leading and trailing edges of the jet. Once the shear layers (originally corresponding to the leading and trailing edges of the jet) collapse, peak turbulent activity is observed toward the centre of the jet.

The peak (absolute) values of the individual terms on the symmetry plane are 29.52 (P_{ii}), 12.83 (T_{ii}), 3.24 (D_{ii}), 5.93 (π_{ii}), 13.22 (ϵ_{ii}) and 8.94 (C_{ii}). The peak values are not observed at the same location. For example, maximum D_{ii} occurs inside the pipe,

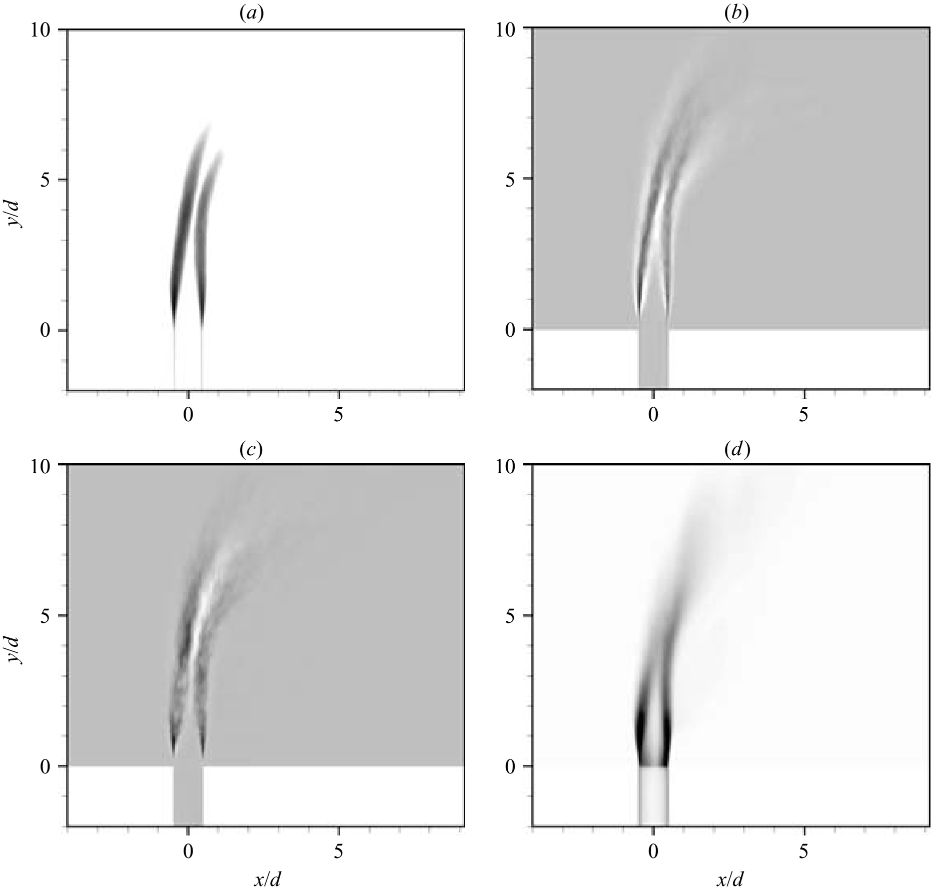

FIGURE 13. Contour plots of kinetic energy budget terms on the symmetry plane. (*a*) P_{ii}, (*b*) T_{ii}, (*c*) π_{ii} and (*d*) ϵ_{ii}.

maximum P_{ii} and ϵ_{ii} occur on the jet edges past the jet exit, and peak values of T_{ii} and π_{ii} are seen further away from the jet exit and roughly near the jet centre – after the shear layers collapse.

In order to assess the relative magnitudes of the terms of the budget, consider locations *A*, *B* and *C*. *A* lies on the leading edge of the jet (and corresponds to peak P_{ii}), while *B* and *C* lie on the centre streamline a few diameters past the jet exit. The relative strengths of the budgets at *A*, *B* and *C* are presented in table 1. The relative strength of the individual budget terms is obtained by normalizing as follows:

$$P'_{ii} = \frac{P_{ii}}{\left(P_{ii}^2 + {T_{ii}}^2 + {D_{ii}}^2 + {\pi_{ii}}^2 + {\epsilon_{ii}}^2 + C_{ii}^2\right)^{\frac{1}{2}}} \; etc. \tag{5.2}$$

At all the locations, viscous diffusion D_{ii} plays a minor role. Turbulent transport (T_{ii}) and the mean convection (C_{ii}) terms are smaller than the production term (P_{ii}) on the jet edge, but are the dominant budget terms at *B*. The pressure transport term (π_{ii}) is the most dominant term at location *C*, but appears to be significantly smaller at the other two locations. Table 1 portrays the difficulty in characterizing turbulence kinetic energy in this flow field. Not only do the characteristics of *k* and the budgets differ between the jet edge and the jet centre but they also vary along the jet length.

(x, y)	A $(-0.47d, 0.85d)$	B $(0.11d, 3.22d)$	C $(0.57d, 5.36d)$
P'_{ii}	0.876	0.102	0.329
T'_{ii}	−0.346	0.693	−0.198
D'_{ii}	−0.013	-3.1×10^{-4}	0.009
π'_{ii}	−0.152	0.119	0.719
ϵ'_{ii}	−0.298	−0.199	−0.519
C'_{ii}	0.011	0.674	0.209

TABLE 1. Comparison of the individual terms of turbulence kinetic energy at three locations: A on the leading edge of the jet, and B and C on the centre streamline.

5.1. *Inside the pipe*

Figure 14 shows the horizontal profiles of the kinetic energy budgets inside the pipe ($y/d = -0.5$), at the jet exit ($y/d = -0.0$) and downstream of the jet exit ($y/d = 0.5$). Examination of profiles at different locations along the length of the pipe showed no differences between $y/d = -2.0$ and $y/d = -0.5$. Hence, profiles at $y/d = -0.5$ indicate the turbulence characteristics upstream of the jet exit, and the profiles exhibit behaviour similar to that of a fully developed turbulent flow in a pipe. The profiles are visibly symmetric about the centre of the pipe. Viscous diffusion balances the dissipation very close to the wall and production peaks slightly away from the wall ($x \sim 0.05d$). All the terms show lower magnitudes toward the centre of the pipe.

The profiles at the jet exit (shown with symbols), however, show markedly different behaviour. The lack of symmetry is apparent, particularly in the profiles of viscous dissipation and mean convection. Both ϵ_{ii} and C_{ii} increase in magnitude across the width of the pipe, and the peak magnitudes are observed closer to the trailing edge. Figure 13 showed significant turbulent activity just past the jet exit. Clearly, this is a result of the interaction between the jet and crossflow fluids. As fluid exits the jet exit, the shear layer expands/enlarges radially and the edges of the jet exhibit an increase in the values of k, P_{ii}, T_{ii}, π_{ii} and ϵ_{ii}. This evolution of the profiles can be observed in figure 14, by comparing profiles of the budgets at $y/d = 0.5$ with those at the jet exit. Within the relatively short distance of $0.5d$, the peak values (of all terms except D_{ii}) increase significantly, while viscous diffusion decreases noticeably. Inside the pipe, π_{ii} is fairly small in magnitude across the pipe diameter. Past the jet exit, the profile shows peaks of significant magnitude near the jet edges. Note the profile of T_{ii}. Edges of the jet are characterized by a negative peak with significant positive peaks on either side. This profile is similar to that observed in a mixing layer (Rogers & Moser 1994), rather than that seen in a turbulent jet (Panchapakesan & Lumley 1993). The disparity between the production and dissipation at the jet exit is indicative of the considerable departure from equilibrium.

5.2. *Downstream of jet exit*

Horizontal profiles of P_{ii} and ϵ_{ii} are shown in figure 15(a) and those of π_{ii} are shown in figure 15(b). These profiles belong to the symmetry plane, and to stations $y/rd = 0.1, 0.5$ and 1.0. The profiles at the first station $y/rd = 0.1$ are characterized by very sharp gradients, corresponding to the leading and trailing edges of the jet. Moving away from the wall, the gradients appear less sharp. Production and dissipation are the dominant terms at all the locations. Viscous diffusion, as mentioned earlier, is relatively negligible. Pressure transport (π_{ii}), while lower than P_{ii} and ϵ_{ii}, is

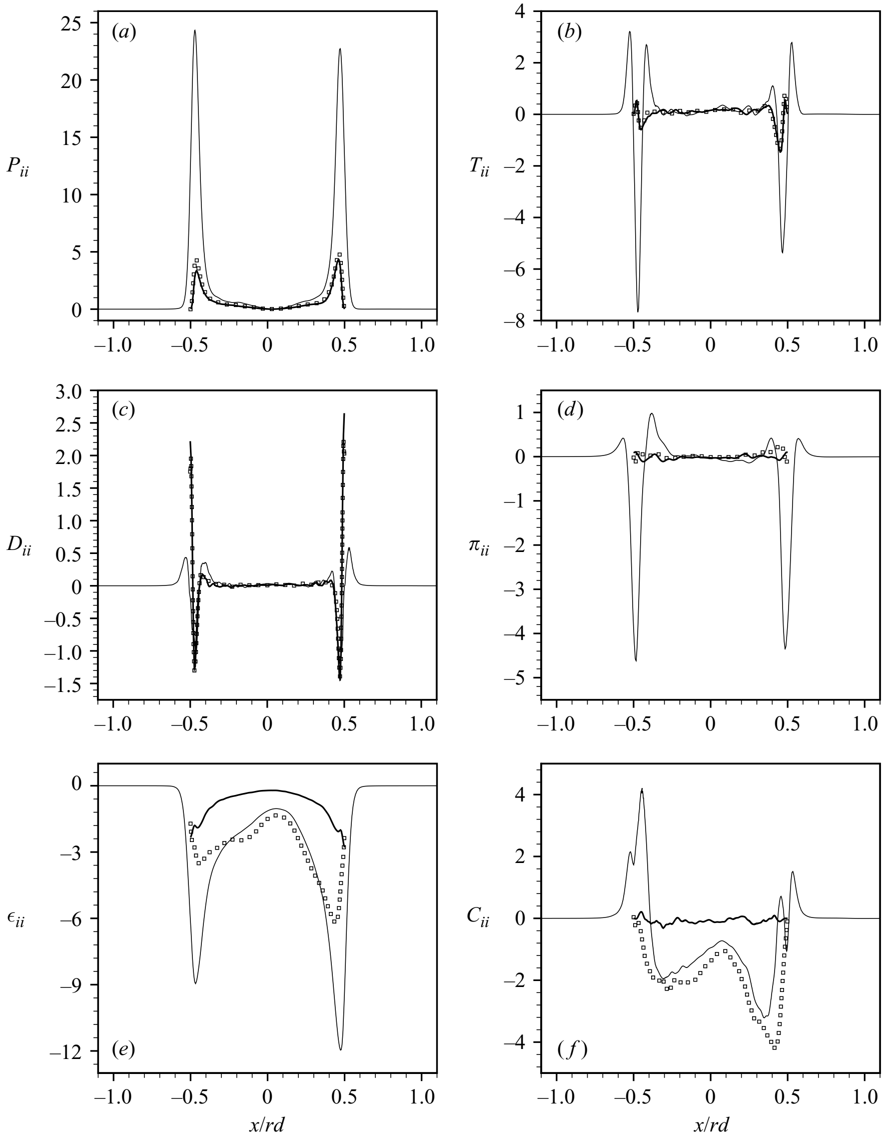

FIGURE 14. Horizontal profiles of the individual budget terms plotted at $y/d = -0.5$ (upstream of the jet exit; thick lines), $y/d = -0.0$ (jet exit; □) and $y/d = 0.5$ (downstream of the jet exit; thin lines).

non-negligible at all the locations in figure 15(*b*). While non-zero values of π_{ii} are observed *only* at the jet edges at $y = 0.1rd$, the profiles show non-zero values *across* the jet width at the other stations. These features are significant to RANS models and will be revisited in section 5.4.

Figure 16 shows trajectory-normal profiles of P_{ii} and ϵ_{ii} with at $s = 5d$, $10d$, $15d$, and $20d$; $n = 0$ indicates the position of the centre streamline. Note that positive n corresponds to the windward side of the jet and a negative n refers to the leeward side. Profiles reflect the increase in jet width along the jet length. Absolute maximum values of the budget terms decrease along the jet. The peak production at $s = 20d$ is

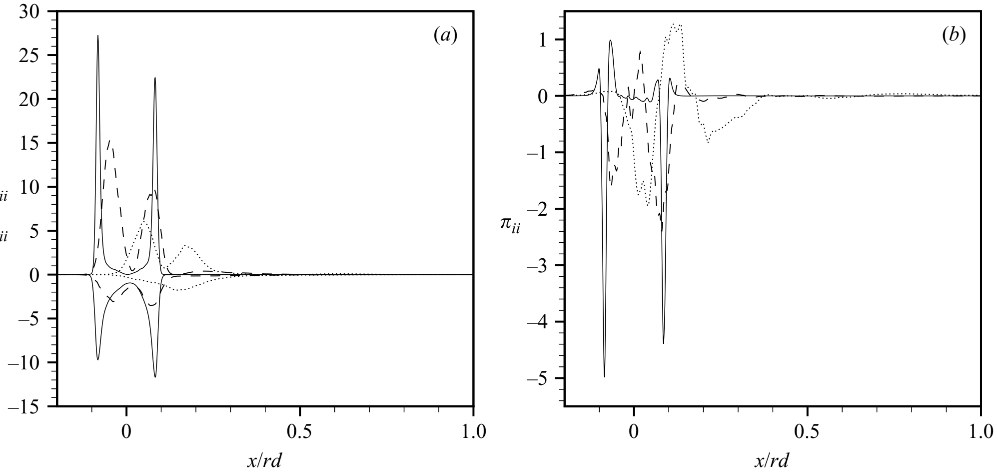

FIGURE 15. Horizontal profiles of the individual budget terms shown at $y/rd = 0.1$ (———), $y/rd = 0.5$ (– – – –) and $y/rd = 1.5$ (········).

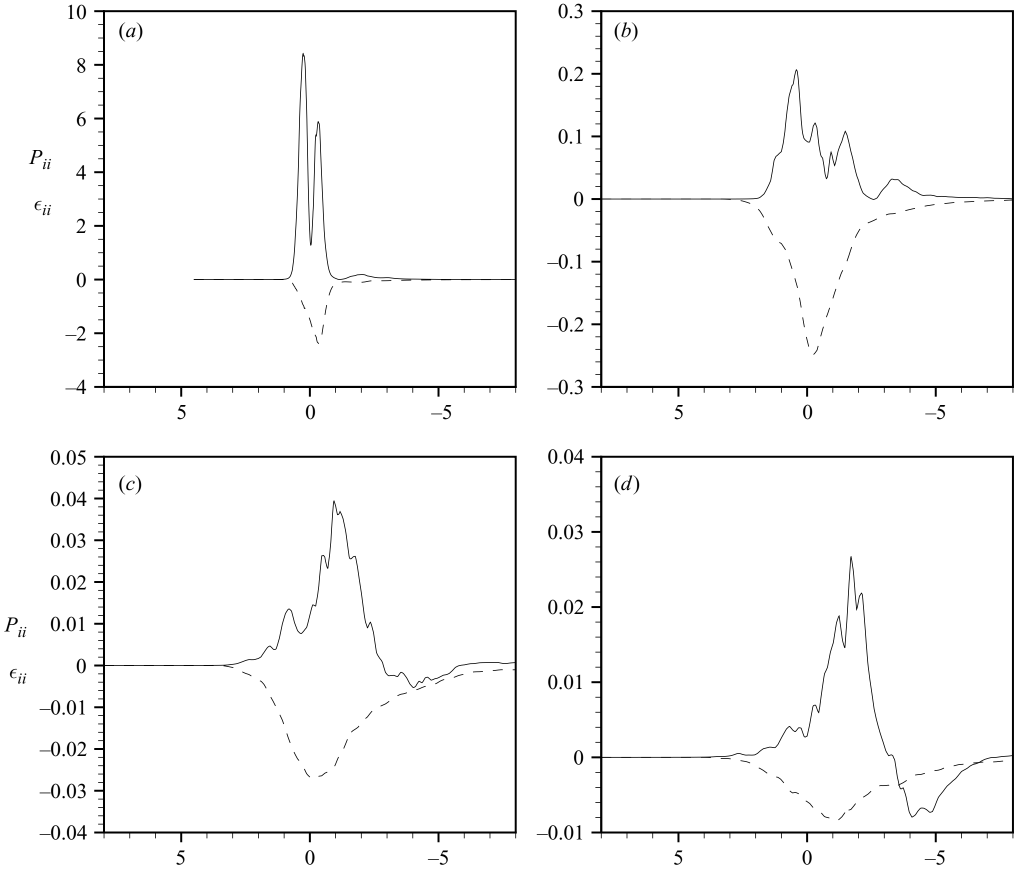

FIGURE 16. Profiles of P_{ii} (———) and ϵ_{ii} (– – – –) along the jet width at (a) $s = 5d$, (b) $s = 10d$, (c) $s = 15d$, and (d) $s = 20d$.

barely 0.5% of the peak production value at $s=5d$. Recall that two-peaked profiles in the near field give rise to single-peaked profiles in the far field. Figure 16(a) indicates that this transition occurs sooner (at a lower s) for dissipation profiles than for production profiles. An important contrast between near field and far field is in regard to locations of peak P_{ii} and ϵ_{ii} in relation to each other. At $s=5d$, peak P_{ii} at the leading edge is higher than that at the trailing edge. As such, location of peak dissipation is to the leeward side of the location of peak production. At $s=15d$ and $s=20d$, in contrast, the location of peak dissipation is observed toward the windward side of peak P_{ii}. In the near field, there exists a high angle of incidence between the crossflow fluid and the jet fluid. The interaction between the jet and crossflow fluids appears to cause peak production of k on the leading edge. In the far field, the direction of the jet is almost the same as that of the crossflow. Recall that the CVP is below the centre streamline and that the jet entrains comparatively more fluid on the leeward side. It appears that due to these features, peak production of k occurs toward the trailing edge of the jet.

5.3. *Time scales and ratios*

Mean flow and turbulent kinetic energy (k, and budgets) characteristics can be used to evaluate the different time scales associated with the flow field. The terminology used here is consistent with that of Pope (2000): $\tau_0=d/u_\infty$ is the reference time scale; τ_ϵ and τ_P are the turbulence decay and turbulence production time scales respectively; τ_ν – the Kolmogorov time scale – indicates the time scale of the smallest turbulent motions and τ_j, the flight time, is an estimate of the time taken by a fluid particle at any location to travel from the jet exit to that location; τ_c is the local convective time scale. These time scales are defined as follows:

$$\tau_0=d/u_\infty, \quad \tau_j=\frac{1}{2}\frac{s}{u_s}, \quad \tau_c=\frac{d}{u_s}, \quad \tau_\nu=\sqrt{\frac{\nu}{\epsilon_{ii}}}, \quad \tau_P=\frac{k}{P_{ii}} \text{ and } \tau_\epsilon=\frac{k}{\epsilon_{ii}}. \tag{5.3}$$

Table 2 provides the representative values of these time scales at a few locations across the domain. The chosen locations are upstream of the jet exit (1 and 2, at the centre of the pipe and at the pipe edge, respectively), just downstream of the jet exit (3, 4 and 5) and locations further away from the jet exit. The objective of this table is to present the different regimes present in this flow. For the sake of reference, these values are compared to relevant data for turbulent jet ($Re=11\,000$; Pope 2000) and turbulent channel ($Re_\tau=180$) flows. Also computed is P/ϵ, which is the ratio of local production of turbulence to the local dissipation. A value of P/ϵ greater than 1.0 indicates transport of turbulence kinetic energy from that location elsewhere, while a value less than 1.0 indicates a transport to that location from elsewhere. The edges of the jet are characterized by P/ϵ values greater than 1.0, and P/ϵ is higher on the leading edge than at the trailing edge along the jet length. It can be inferred that turbulence kinetic energy produced at the jet edges is transported toward the centre of the jet, where $P/\epsilon<1.0$. Peak P/ϵ (across the domain) is observed at the leading edge of the jet, at $s=rd$. This point corresponds to the location of significant change in direction of the jet fluid. The jet is fairly vertical upstream of this point and bends considerably, into the crossflow, downstream of this point.

5.3.1. *Locations of maximum P_{ii} and ϵ_{ii}*

Figure 17(a) shows the locus of the local maximum production of turbulent kinetic energy, compared to the local maxima of the viscous dissipation. For comparison, the centre streamline is also plotted. While the differences are small, these trajectories

	τ_j	τ_c	τ_ν	τ_ϵ	τ_P	P/ϵ
Upstream jet exit						
1. Near-wall ($x/d=-0.46$)		0.268	0.025	0.285	0.149	1.916
2. Pipe centre		0.133	0.079	0.619	21.514	0.029
Downstream jet–exit						
$s/rd=0.1$						
3. Leading edge	0.093	0.327	0.011	0.177	0.063	2.817
4. Jet centre	0.038	0.134	0.033	0.232	9.093	0.0255
5. Trailing edge	0.082	0.289	9.88×10^{-3}	0.148	0.077	1.929
$s/rd=1.0$						
6. Leading edge	1.133	0.394	0.041	2.823	0.324	8.714
7. Jet centre	0.795	0.276	0.029	1.412	2.172	0.650
8. Trailing edge	1.041	0.362	0.026	1.023	0.543	1.883
Far field						
9. $s/d=15.0$	6.336	0.845	0.207	4.01	8.855	0.452
10. $s/d=$ 20.0	9.350	0.935	0.440	10.196	21.117	0.483
Other flows						
11. Regular jet ($r/r_{1/2}=0.7$)	5.3			4.5	5.7	0.8
12. Channel ($y^+=11.8$)		0.1006	0.0156	0.225	0.124	1.81

TABLE 2. Ratios and time scales in the flow, at a few locations. Compared with relevant available turbulent jet and channel flow data. All the time scales are normalized with τ_0.

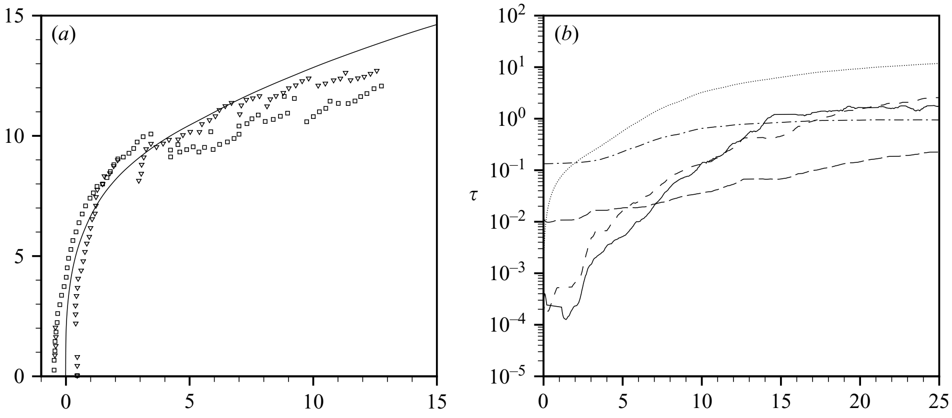

FIGURE 17. (*a*) Trajectory of local maximum P_{ii} (□) compared to trajectory of local maximum ϵ_{ii} (△). Also shown is the centre streamline trajectory (———). (*b*) Time scales in the flow, as a function of distance s from the jet exit. ———, τ_P; – – – –, τ_ϵ; ········, τ_j; —·—, τ_c; and — — —, τ_ν.

are different from each other. An indication of this behaviour can be seen from the profiles at $y=0.5d$ in figure 14. Profiles for both production and dissipation are characterized by two peaks corresponding to the leading edge and the trailing edge. However, peak P_{ii} is observed at the leading edge while the peak ϵ_{ii} is observed on the trailing edge. A similar difference in the locations of peak production and dissipation are also observed in figure 15(*a*).

The variation of different time scales along the jet length is plotted in figure 17(*b*). A straightforward approach would be to compute the time scales (5.3) at all points along a single curve (e.g. the centre streamline). Consider a point close to the jet exit, on the centre streamline. Both P_{ii} and ϵ_{ii} are characterized by low values compared to that at the jet edges, as seen from figure 14. Clearly, τ_P and τ_ϵ computed at this location would not be indicative of the turbulence time scales at this particular distance from the jet exit. In addition, one would expect large errors due to small denominators (either P_{ii} or ϵ_{ii}). Profiles in figure 17(*b*) are plotted, in order to circumvent this issue, along lines of local maxima of the denominators. That is, τ_j and τ_c are computed along the centre streamline (where u_s would be expected to be maximum), τ_P is computed along the trajectory of local maximum production, and τ_ν and τ_ϵ are computed along the trajectory of local maximum dissipation. Figure 17(*b*) shows that all the time scales involved with the flow increase with distance from the jet exit. Curves plotting τ_P and τ_ϵ are fairly close to each other, indicating that rates of production and dissipation of turbulence are similar. Both these time scales are much lower than τ_ν close to the jet exit. The increase of τ_P and τ_ϵ with s, however, is faster than that of τ_ν, and the Kolmogorov time scale is the smallest of the timescales past $s \sim 8d$.

A few words regarding the computation of kinetic energy budgets follow. Consider (5.1). The budget is said to be balanced if the storage term $\partial k/\partial t = P_{ii} + T_{ii} + D_{ii} + \pi_{ii} + \epsilon_{ii} - C_{ii}$ is zero. The magnitude of the storage term, theoretically zero, is a measure of the numerical fidelity and convergence of the solution. The storage term is not necessarily small if the discrete operators used to compute the budgets are not consistent with the operators used to solve the Navier–Stokes and pressure equations. In order to achieve such a consistency, discrete Navier–Stokes and time-averaged Navier–Stokes equations were used to obtain discrete equations for u_i. These were contracted with u_i to obtain the discrete kinetic energy budget terms. The operators/expressions were validated by computing budgets for a turbulent channel ($Re_\tau = 180$) and comparing the results with that of Moser, Kim & Mansour (1999). Good agreement was observed. Computation of budgets in a homogeneous flow is comparatively easier on account of spatial averaging. For a jet in crossflow, in contrast, the lack of any homogeneous direction demands that the balance be reduced only through time averaging.

In the present simulation, the balance was computed at every mesh point along with the budgets. The balance, normalized according to (5.2), was examined across the domain. Inside the pipe, the maximum normalized balance was observed to be about 0.6%. At the jet exit, the highest value was observed closer to the trailing edge, at about 0.8%. Downstream of the jet exit, the highest values were seen to be about 1.02%, 2.0%, 1.7% and 1.9% at locations $y/rd = 0.1$, 0.5, 1.0 and 1.5 respectively. For the sake of comparison, budgets from a turbulent channel flow simulation ($Re_\tau = 180$; Moser *et al.* 1999) were similarly normalized, and the maximum value for the balance was found to be 0.35% and is observed at $y^+ = 5.5$. Note that this is after spatial and temporal averaging on a mesh containing 128 points in the streamwise and spanwise directions.

5.4. *Modelling implications*

The Reynolds-Averaged Navier–Stokes (RANS) equations have been widely used to simulate transverse jets. On investigating the effectiveness of several models, Hoda &

Acharya (2000) conclude that existing models provide overly simplistic predictions for the complex flow field. Even modelling attempts that predict the flow field fairly well across the domain are found to be unsatisfactory in the near field. For example, Garg & Gaugler (1997) obtain good results except near the injection rows and the leading edge regions using a Baldwin–Lomax model. A systematic study of film cooling by Demuren, Rodi & Schonung (1986) showed that turbulent mixing in this flow is poorly represented by the eddy viscosity model. Hoda & Acharya state that simple expressions for ϵ in k–ϵ models are inadequate in the jet region (with high gradients in all directions), and mention the need to optimize the ϵ budget, on the lines of the DNS-based model by Rodi & Mansour (1993).

This section is an attempt at using the present DNS results to explain why typical RANS computations experience difficulties in predicting this flow. The results presented in this paper show that the flow field is far from being in turbulent equilibrium. In particular, this behaviour is seen near the jet exit and in the near field, as seen from figures 14 and 15 respectively. Further, the flow field is three-dimensional and non-isotropic. The non-isotropic nature of the flow has prompted the use of nonlinear models instead of linear models. Hoda & Acharya report that the nonlinear models (Mayong–Kasagi and Speziale models) do not provide significantly better predictions than the linear models. They suggest the reason to be that the coefficients of the nonlinear models are obtained from simple wall-bounded flows. Clearly, the turbulence and the anisotropic characteristics in jets in crossflow are significantly more complex. It was shown in § 5 that while the flow upstream of the jet exit showed characteristics of a turbulent pipe flow, the flow field downstream of the jet exit shows few, if any, similarities.

Reynolds-stress transport models (RSTM) are expected to account for anisotropy in the flow and hence predict the flow better than isotropic models. Acharya *et al.* (2001) point that RSTM predictions are not substantially better than two-equation model predictions. In most Reynolds-stress transport models, the transport of turbulence kinetic energy by pressure (π_{ii}) is either ignored or modelled along with T_{ii} (Pope 2000). In simple wall-bounded flows, π_{ii} is identically zero near the walls and fairly small across the domain. In a mixing layer, the pressure transport is important only near the edge of the layer (Rogers & Moser 1994), and is relatively small over most of the layer. Application of RSTM, hence, appears reasonable for such simple flows. However, in a jet in crossflow, π_{ii} is not negligible. There are regions of flow (table 1) where π_{ii} is not only significant but is also higher in magnitude than the rest of the budget terms. Profile of π_{ii} at $y = rd$ (figure 15*b*) shows significant magnitude across the jet width. It must be expected that any model that assumes little or no impact of π_{ii} on k would result in an unsatisfactory prediction of this flow.

A final point about RANS modelling of a transverse jet regards the computational mesh and the domain. The profiles (of intensities k, and budget terms) involve steep gradients at the jet edges. Computations with inadequate resolution in this region, hence, would be inaccurate. Also, most RANS simulations do not include the pipe in the computational domain. Muppidi & Mahesh (2005) and Yuan *et al* (1999) mentioned the sensitivity of the flow field to the boundary conditions of the jet. Inclusion of the pipe appears necessary for any transverse jet simulation (RANS, LES or DNS). Figure 14 showed that the budgets at the jet exit have non-trivial profiles. Therefore, it appears that a RANS computation that does not include the pipe would have to prescribe, in addition to the mean velocities, complex boundary conditions for k and ϵ_{ii} across the jet exit.

6. Summary

A direct numerical simulation of a round turbulent jet in crossflow, at conditions of experiments by Su & Mungal (2004), is performed. Velocity and turbulent intensity profiles from the simulation are compared to those from the experiments, and the observed agreement is good. The flow is observed to be three-dimensional and involves a wide range of scales of motion. The deformation of the jet, from a circular cross-section to a kidney shape, begins with the flattening of the trailing edge close to the jet exit. The counter-rotating vortex pair is displaced from the centre streamline along the leeward side. A trajectory based on vorticity is therefore lower than a trajectory based on the centre streamline. Streamlines indicate that crossflow fluid, near the symmetry plane, travels around the jet and is entrained on the downstream side. Also, jet fluid off the symmetry plane is deposited below the centre streamline on the symmetry plane. Contours of instantaneous vorticity, profiles of mean velocity ($\overline{v}$) and spanwise intensity ($\overline{w'w'}$) reflect this. An examination of turbulent kinetic energy budget for this flow shows that the flow is not in turbulent equilibrium. The near field is characterized by P/ϵ values greater than 1.0 along the jet edges and less than 1.0 along the jet centre. Jet and crossflow fluid interaction in the near field causes peak production of turbulent kinetic energy on the leading edge of the jet. In the far field, entrainment of crossflow fluid and the CVP cause peak production below the centre streamline. Steep (velocity/intensity/budget) gradients, non-equilibrium behaviour and non-trivial budget profiles at the jet exit make RANS computations of turbulent transverse jets formidable.

This work was supported by the National Science Foundation under grant CTS–0133837. Computer time was provided by the National Center for Supercomputing Applications (NCSA), Minnesota Supercomputing Institute (MSI) and the San Diego Supercomputer Center (SDSC). The authors thank professors Godfrey Mungal and Lester Su for providing their experimental data and for useful discussions.

REFERENCES

Acharya, S., Tyagi, M. & Hoda, A. 2001 Flow and heat transfer predictions for film-cooling. *Ann. NY Acad. Sci.* **934**, 110–125.

Andreopoulos, J. & Rodi, W. 1984 Experimental investigation of jets in a crossflow. *J. Fluid Mech.* **138**, 93–127.

Babu, P. & Mahesh, K. 2004 Upstream entrainment in numerical simulation of spatially evolving round jets. *Phys. Fluids* **16**, 3699–3705.

Broadwell, J. E. & Breidenthal, R. E. 1984 Structure and mixing of a transverse jet in incompressible flow. *J. Fluid Mech.* **148**, 405–412.

Chochua, G., Shyy, W., Thakur, S., Brankovic, A., Lienau, K., Porter, L. & Lischinsky, D. 2000 A computational and experimental investigation of turbulent jet and crossflow interaction. *Numer. Heat Transfer*, Part A **38**, 557–572.

Demuren, D. K., Rodi, W. & Schonung, B. 1986 Systematic study of film cooling with a three-dimensional calculation procedure. *Trans. ASME: J. Turbomach.* **108**, 124–130.

Eggels, J. G. M., Unger, F., Weiss, M. H., Westerweel, J., Adrian, R. J., Friedrich, R. & Nieuwstadt, T. M. 1994 Fully developed turbulent pipe flow: A comparison between numerical simulation and experiment. *J. Fluid Mech.* **268**, 175–209.

Fearn, R. L. & Weston, R. P. 1974 Vorticity associated with a jet in crossflow. *AIAA J.* **12**, 1666–1671.

Fric, T. F. & Roshko, A. 1994 Vortical structure in the wake of a transverse jet. *J. Fluid Mech.* **279**, 1–47.

Hasselbrink, E. F & Mungal, M. G. 2001 Transverse jets and jet flames. Part 1. Scaling laws for strong transverse jets. *J. Fluid Mech.* **443**, 1–25.

Hoda, A. & Acharya, S. 2000 Predictions of a film coolant jet in crossflow with different turbulent models. *Trans. ASME: J. Turbomach.* **122**, 558–569.

Garg, V. K. & Gaugler, R. E. 1997 Effect of coolant temperature and mass flow on film cooling of turbine blade. *Intl J. Heat Mass Transfer* **2**, 435–445.

Kamotani,Y. & Greber, I. 1972 Experiments on turbulent jet in a crossflow. *AIAA J.* **10**, 1425–1429.

Karagozian, A. R. 1986 An analytical model for the vorticity associated with a transverse jet. *AIAA J.* **24**, 429–436.

Keffer, J. F. & Baines, W. D. 1963 The round turbulent jet in a cross wind. *J. Fluid Mech.* **15**, 481–496.

Kelso, R. M., Lim, T. T & Perry, A. E. 1996 An experimental study of round jets in cross–flow. *J. Fluid Mech.* **306**, 111–144.

Kelso, R. M. & Smits, A. J. 1995 Horseshoe vortex systems resulting from the interaction between a laminar boundary layer and a transverse jet. *Phys. Fluids* **7**, 153–158.

Krothapalli, A., Lourenco, L. & Buchlin, J. M. 1990 Separated flow upstream of a jet in a crossflow. *AIAA J.* **28**, 414–420.

Mahesh, K., Constantinescu, G. & Moin, P. 2004 A numerical method for large-eddy simulation in complex geometries. *J. Comput. Phys.* **197**, 215–240.

Margason, R. J. 1993 Fifty years of jet in crossflow research. In *AGARD Symp. on a Jet in Cross Flow, Winchester, UK AGARD CP*-534.

Moser, R. D., Kim, J. & Mansour, N. N. 1999 Direct numerical simulation of turbulent channel flow up to $Re_\tau = 590$. *Phys. Fluids* **11**, 943–946.

Muppidi, S. & Mahesh, K. 2005 Study of trajectories of jets in crossflow using direct numerical simulations. *J. Fluid. Mech.* **530**, 81–100.

Panchapakesan, N. R. & Lumley, J. L. 1993 Turbulence measurements in axisymmetric jets of air and helium. Part 1. Air jet. *J. Fluid Mech.* **246**, 197–223.

Pope, S. B. 2000 *Turbulent Flows*. Cambridge University Press.

Pratte, B. D. & Baines, W. D. 1967 Profiles of the round turbulent jet in a cross flow. *J. Hydraul. Div., ASCE* **92**, 53–64.

Rodi, W. & Mansour, N. N. 1993 Low Reynolds number k–ϵ modelling with the aid of direct simulation data. *J. Fluid Mech.* **250**, 509–529.

Rogers, M. M. & Moser, R. D. 1994 Direct simulation of a self-similar turbulent mixing layer. *Phys. Fluids* **129**, 547–572.

Schlichting, H. T. 1968 *Boundary Layer Theory*. McGraw-Hill.

Schluter, J. U. & Schonfeld, T. 2000 LES of jets in crossflow and its application to a gas turbine burner. *Flow Turbulence Combust.* **65**(2), 177–203.

Sherif, S. A. & Pletcher, R. H. 1989 Measurements of the thermal characteristics of heated turbulent jets in cross flow. *Trans. ASME: J. Heat Transfer* **111**, 897–903.

Smith, S. H. & Mungal, M. G. 1998 Mixing, structure and scaling of the jet in crossflow. *J. Fluid Mech.* **357**, 83–122.

Su, L. K. & Mungal, M. G. 2004 Simultaneous measurement of scalar and velocity field evolution in turbulent crossflowing jets. *J. Fluid Mech.* **513**, 1–45.

Yuan, L. L. & Street, R. L. 1998 Trajectory and entrainment of a round jet in crossflow. *Phys. Fluids* **10**, 2323–2335.

Yuan, L. L., Street, R. L. & Ferziger, J. H. 1999 Large-eddy simulations of a round jet in crossflow. *J. Fluid Mech.* **379**, 71–104.